ELSEVIER

Thin Solid Films 409 (2002) 88–97

thin solid films

www.elsevier.com/locate/tsf

# Investigation of an upflow cold-wall CVD reactor by gas phase Raman spectroscopy

Chinho Park[a,*], Jang Yeon Hwang[b], Min Huang[b], Timothy J. Anderson[b]

[a]*School of Chemical Engineering and Technology, 214-1 Tae-dong, Kyongsan 712-749, South Korea*
[b]*University of Florida, Department of Chemical Engineering, Gainesville, FL 32611, USA*

**Abstract**

The gas phase dynamics of an inverted, stagnation point flow CVD reactor were studied by both experiment and modeling. The axial centerline temperature profile in the reactor was measured by analysis of the rotational Raman spectra from the carrier gas ($N_2$ or $H_2$) as a function of the inlet flow velocity and the reactor aspect ratio. It was found that a larger temperature gradient normal to the susceptor surface was obtained with higher gas flow velocity, larger aspect ratio, and the use of a $N_2$ carrier gas. A two-dimensional axisymmetric model with detailed heat transfer descriptions predicted the experimental data well. The validated model clearly demonstrates that recirculation flows are less likely in inverted reactor geometry. 

*Keywords:* Chemical vapor deposition; Gas phase Raman spectroscopy; Stagnation point flow reactor; Two-dimensional axisymmetric model

## 1. Introduction

Cold-wall chemical vapor deposition (CVD) reactors are often used to deposit thin films. In particular, organometallic vapor phase epitaxy (OMVPE) is widely used for depositing epitaxial films of compound semiconductors and their alloys [1,2]. Since CVD reactors are commonly operated in the mass transport limited regime, the quality and uniformity of the deposited layers are strongly influenced by the gas dynamics. It is beneficial to establish a uniform flow field in the reactor that is free of laminar vortices to minimize the reactant switching time. Gas phase isotherms parallel to the substrate are also desirable to improve growth uniformity. Additionally, a large normal thermal gradient in the vicinity of the substrate minimizes parasitic gas phase reactions and reduces particle impingement rates. A large temperature gradient normal to the substrate surface can, however, lead to recirculation flow patterns in the reactor, causing growth rate variations, delayed impurity incorporation, and graded heterojunctions [3]. These issues have been addressed in several modeling and experimental investigations [4–7] of conventional reactor geometries (e.g. horizontal, vertical downflow, and rotating disk configurations).

This study reports both experimental temperature profiles and two-dimensional modeling results for an unconventional upflow, stagnation point reactor geometry. With this configuration, a stabilizing density gradient is expected, thereby reducing or eliminating flow recirculation effects frequently encountered in conventional geometries at otherwise similar operating conditions. In addition, particulate impingement effects should be reduced because of the favorable alignment of the reactor with respect to gravity. This reactor geometry is also suited for experiments to extract kinetic data, given the relatively well-defined flow and temperature fields in the reactor. Wafer mounting onto the inverted susceptor, of course, would be more difficult than in the non-inverted designs.

Stagnation point flow reactors have been investigated by several workers and their results have shown that the reactor orientation strongly affects the extent of natural convection produced by thermal gradients in the gas phase [7–14]. Numerical calculations have suggested that natural convection driven cells can be reduced by increasing the inlet flow rate, rotating the susceptor, reducing the reactor pressure, reshaping the reactor wall, decreasing the distance between the inlet and the sus-

*Corresponding author. Tel.: +82-53-810-2522; fax: +82-53-814-8790.

*E-mail address:* chpark@yu.ac.kr (C. Park).

0040-6090/02/$ - see front matter 
PII: S0040-6090(02)00109-8

ceptor, introducing baffles or inverting the reactor [5,15,16].

The importance of the approach used to describe the heat transfer in the reactor model was emphasized in explaining discrepancies between the observed and predicted growth rate of GaAs in a vertical upflow OMVPE reactor [10]. Chinoy et al. [8] investigated the factors controlling the flow and temperature fields in a vertical upflow OMVPE reactor (e.g. susceptor temperature, susceptor-nozzle distance, gas flow rate and reactor pressure), and radiative heat transfer rates were found to be comparable to those by convection. These modeling studies point to the sensitivity of the results to model assumptions (e.g. thermal boundary conditions) and constitutive equations, and there exists very little experimental data exist beyond growth rates to validate reactor models.

In this study, axial centerline temperature profiles were measured in a vertical upflow, cold-wall CVD reactor by gas phase Raman spectroscopy, and the results were compared with numerical calculations. The axial centerline temperature profiles near the susceptor surface were measured by analysis of the pure rotational Raman spectra from the carrier gas molecules, $N_2$ or $H_2$ as a function of the inlet flow velocity and the reactor aspect ratio. A two-dimensional axisymmetric model was developed and used to predict the temperature profiles and velocity fields at the experimental conditions.

## 2. Experimental details

A schematic of the reactor geometry is shown in Fig. 1. A feature of this reactor design is the provision for a sweeping gas flow to minimize wall deposition of precursors or reaction products, although no reactants were introduced in this study. The reactor body was made of optically flat quartz with a square cross-section to reduce position-dependent intensity variations of the Raman signal from irregular surface scattering. A cylindrical quartz tube was inserted into the reactor to simulate a practical geometry and simplify the reactor model. Four vertical slits, each separated by 90°, were opened in this tube and were positioned symmetrically with respect to the axial centerline of the reactor. These slits permitted access of the laser beam to the reactor centerline and detection of the scattered light. The reactor bottom and top flanges were made of 316 stainless steel and contained recessed grooves (square), in which O-rings were placed to seal the quartz reactor.

A resistance heater assembly was inserted through the top plate of the reactor and served as the susceptor. The body of the furnace was a cylindrical quartz tube (3.8 cm O.D.), and a vacuum ($<10^{-5}$ Torr) was maintained inside the tube to insulate the heating block from the surroundings. The heating block rested on the inside bottom of the quartz furnace body. The set point temperature of the furnace was measured by a type-K thermocouple embedded in the heating block, and the set point temperature was controlled at 650 °C for all experiments. The details of the furnace design are described elsewhere [17].

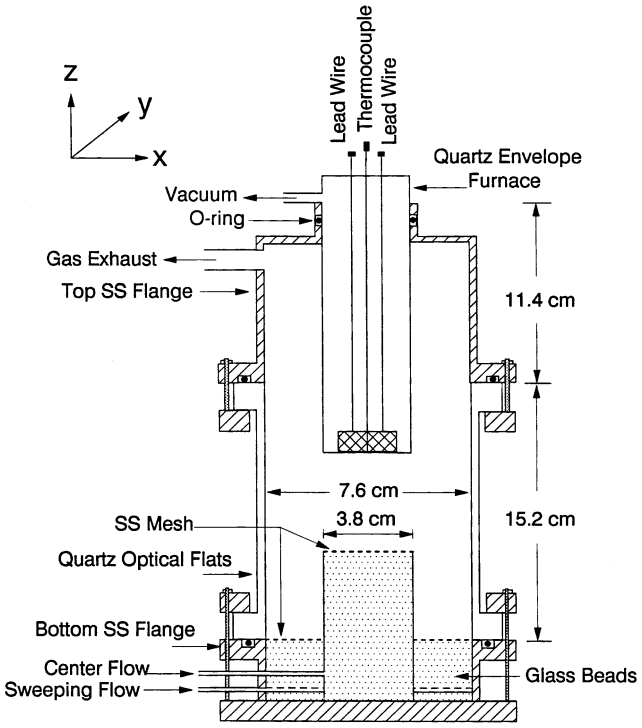


Fig. 1. Schematic of the stagnation point upflow reactor.

The reactor aspect ratio (AR), which is defined as the ratio of the distance between the susceptor and the center inlet tube to the center tube diameter (3.386 cm I.D.), could be varied by moving the furnace assembly to achieve a maximum value of AR = 2. The carrier gas, $N_2$ or $H_2$, was introduced into the reactor through the center and outer inlet tubes simultaneously. To promote uniform flow, a capped spiral tube manifold with small gas exit holes was placed in the bottom of the sweeping gas inlet tube. Stainless steel meshes were placed on top of both inlet tubes which were packed with 3 mm diameter glass beads to provide a nearly flat velocity profile at each gas inlet. The entire reactor was situated in the macro-chamber of the Raman system, and the reactor could be translated in three directions by a micrometer controlled $x$–$y$–$z$ stage. For these studies, the operating pressure of the reactor was maintained at atmospheric pressure.

A Ramanor U-1000 Raman spectrometer (Jobin Yvon) was used to collect and analyze the scattered light in a 90° configuration. The excitation laser beam was introduced in the $-x$ direction (Fig. 1) and the scattered light was detected in the $+y$ direction, forming an $x$–$y$ scattering plane. The 488 nm line of a cw argon

ion laser was used as the excitation source at a laser power of 1 W. Polarization of the incident laser was in the $z$ direction, but the scattered light polarization was not analyzed in these experiments. A photomultiplier tube (PMT) was used as a detector, and photon counting electronics were employed.

The temperature distribution along the reactor centerline was measured by collecting and analyzing the pure rotational Raman scattered light from the carrier gas. This technique has the advantage of not disturbing the flow field as compared to the use of a thermocouple [18], and it provides a spatial resolution in three dimensions better than interference holography [19]. In this study, spatial resolutions of approximately 30 μm in the $y$ and $z$ directions and approximately 3000 μm in the $x$ direction could be obtained, where the values were calculated with the assumption of a focal cylinder [20]. The origin was determined by monitoring the scattered light intensity decrease as the susceptor began to block the effective area of sight of the collection lens upon translation of the laser beam in the $+z$ direction. The position at which the intensity of the strongest rotational Raman band of the carrier gas decreased by 5% was used to calculate the surface position. With the well-defined optical dimensions of the macro-chamber, the origin was reproducibly determined to within 0.1 mm.

The theory of Raman scattering is very well developed for diatomic gases [20]. Assuming the rotational modes are at thermal equilibrium, the scattering intensities for rotational Raman scattering from an assembly of randomly oriented diatomic molecules can be described by explicit expressions [21]. The assumption of thermal equilibrium is reasonable in this study since both the temperature and pressure are high.

The Raman spectra were obtained with a resolution of 1.5 $cm^{-1}$ and an integration time of 1 s. Spectrometer frequencies were calibrated by the neon emission line at 5400.6 Å. In the case of $N_2$, transitions from $J=0$–20 were clearly observed, where $J$ represents the rotational quantum number of the initial level for the Stokes band and the final level for the anti-Stokes band. For $N_2$, the Stokes bands alone were sufficient to determine the temperature. For $H_2$, however, only four Stokes and two anti-Stokes bands had a sufficiently large signal-to-noise ratio to be useful. Thus, all six bands were included in the analysis to determine temperature.

The data obtained in this study showed the expected relationship, indicating that the assumption of a Boltzmann population of the occupied rotational energy levels was reasonable. The accuracy of the measured temperature depends on the signal-to-noise ratio, which decreases with increasing temperature. When the furnace temperature was higher than 800 °C, radiation from the heating block increased the noise level, especially when the laser probe was near the susceptor surface. At the furnace temperature of this study (650 °C), the radiation from the susceptor was reduced, and the spectra obtained showed reasonable signal-to-noise ratios (>8:1). The uncertainty of the temperature, defined as one standard deviation (1 S.D.) was calculated from the goodness of fit to the explicit expressions [21] and was less than ±20 °C for most measurements of this study. The temperature of $N_2$ was more accurately determined than that of $H_2$, because more data were available for $N_2$.

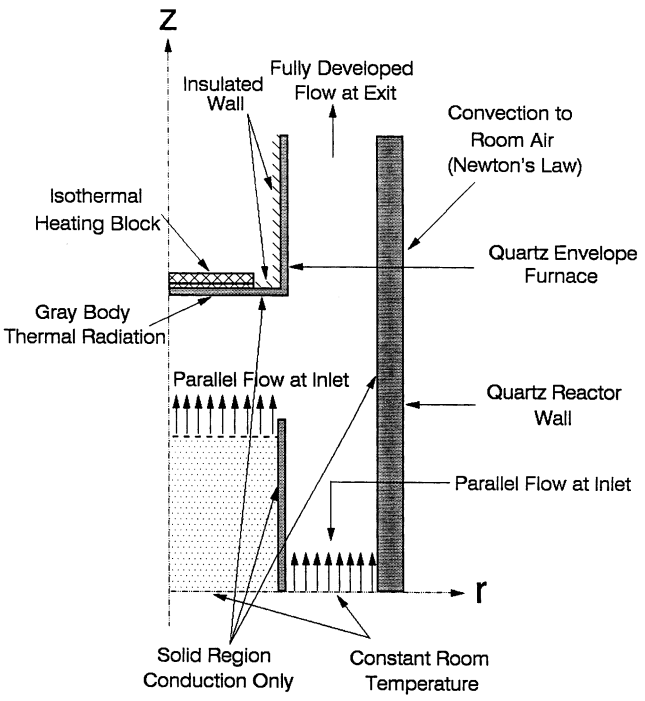


Fig. 2. Schematic of the reactor model used in the numerical calculations.

## 3. Reactor modeling and simulation

A two-dimensional axisymmetric model was developed to describe the experimentally observed temperature profiles. A schematic of the reactor model is shown in Fig. 2 along with the boundary conditions. Several assumptions were incorporated in the model formulation to reduce the scale of the numerical calculations. First, the time dependent terms in the governing equations were neglected, since data were collected only after the gases had flowed for long times. The assumption of an axisymmetry (i.e. 2-D in $r$ and $z$) has been shown to be valid for vertical reactors except under conditions where strong natural convection exists [5]. The Reynolds number in each experiment was less than 250 for $N_2$ and 70 for $H_2$, and thus, laminar flow was assumed. The carrier gas is assumed to be an ideal gas but with no effect of pressure on density (Mach number $\ll 1$). With these assumptions, equations of change were constructed in cylindrical coordinates. The energy equation neglected the viscous heating term. The temperature

dependence of the gas viscosity and thermal conductivity was assumed to follow a power law [15]:

$$\mu = \mu_0 (T/T_0)^{0.648} \quad (1)$$

$$k = k_0 (T/T'_0)^{0.691} \quad (2)$$

where the parameters $\mu_0$, $T_0$, $k_0$, and $T'_0$ were taken as [22], $\mu_0 = 1.781 \times 10^{-5}$ kg m$^{-1}$ s$^{-1}$ at $T_0 = 300.55$ K and $k_0 = 2.6108 \times 10^{-2}$ J m$^{-1}$ s$^{-1}$ K$^{-1}$ at $T'_0 = 299.85$ K for $N_2$ and $\mu_0 = 0.876 \times 10^{-5}$ kg m$^{-1}$ s$^{-1}$ at $T_0 = 293.58$ K and $k_0 = 1.8674 \times 10^{-1}$ J m$^{-1}$ s$^{-1}$ K$^{-1}$ at $T'_0 = 299.85$ K for $H_2$. The temperature dependence of the heat capacity $c_p$ for each species was obtained from interpolation of the experimental data [23].

A no-slip condition was applied at all solid boundaries. At both the center and sweeping flow inlets, a one-dimensional flow and uniform velocity profile were assumed. At the outlet (12.4 cm beyond the susceptor surface), the velocity and temperature fields were assumed to be fully developed. This assumption was substantiated by confirming that the calculated velocity profile did not vary when the exit length increased. The center and sweeping flows were assumed to enter the bottom of the reactor at room temperature.

The side wall of the furnace was assumed to be insulated. The furnace wall, center inlet tube wall and reactor wall were included in the computational domain. It was assumed that conduction was the only heat transfer mechanism in those areas. The gray body radiation heat transfer from the susceptor surface was also included in the calculation with a constant emissivity value of 0.3 [24], and the view factors were calculated by the method described by Siegel and Howell [25]. The outside of the reactor was blanketed with room-temperature air, and the heat transfer rate was assumed to obey Newton's law.

A Penalty Finite Element Method was used to perform the numerical simulations, and the code developed in this study was validated by comparing the solution of the driven cavity flow problem to the published numerical solution [26]. The reactor was divided into six calculation zones: the heating block inside the quartz envelope furnace, the quartz envelope furnace wall, the gas volume in the reactor, the inside of the center inlet tube filled with glass beads, the stainless steel center inlet tube wall, and the quartz reactor wall. Each zone was placed in a single simulation domain, incorporating the appropriate physical properties. The mesh size was different for each zone (minimum $0.53 \times 0.39$ mm$^2$ and maximum $1.28 \times 5.67$ mm$^2$), generating a total of 6670 rectangular two-dimensional elements. For the center inlet tube zone, it was assumed that the glass beads and the gas flow were at thermal equilibrium, and therefore, the gas temperature was equal to that of the glass beads at each element node.

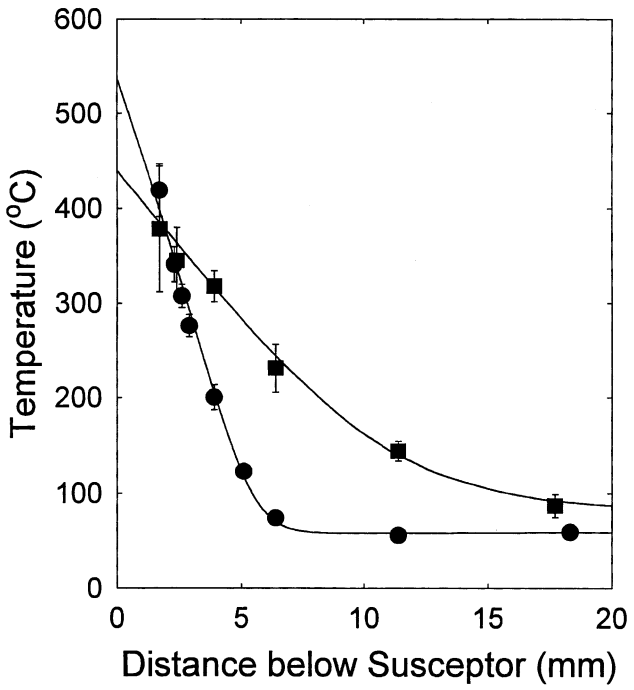


Fig. 3. Axial centerline temperature profile in the reactor for $N_2$ (●) and $H_2$ (■). Calculated results (solid lines) are shown with the experimental data: AR = 1, $T_{set}$ = 650 °C.

For each iteration, the velocity components and temperature were solved simultaneously given initial guesses. The temperature distribution was then used to upgrade the density as well as the viscosity, thermal conductivity and heat capacity. Because the pressure variation in the reactor is much less than the pressure itself, it was assumed that the density was a function only of temperature and could be determined from the state equation of an ideal gas. The calculation was repeated until a converged solution was obtained. Calculations were carried out on an IBM compatible personal computer, typically requiring approximately 60 iterations.

## 4. Experimental results and discussion

The axial centerline temperature profile in the reactor was measured for both $N_2$ and $H_2$ carrier gases as a function of the inlet gas flow velocity and the aspect ratio. Fig. 3 shows the axial temperature profile in the reactor for both $N_2$ and $H_2$ carrier gases at the same operating conditions (i.e. a gas inlet velocity of 3.0 cm/s for both the center and the sweeping flows, AR = 1, and 650 °C susceptor set point temperature). These results clearly show that the use of an $N_2$ carrier gas produces a steeper temperature gradient normal to the susceptor surface than the use of a $H_2$ carrier gas. The same behavior was obtained by other investigators using both horizontal [4,6,27–31] and vertical downflow

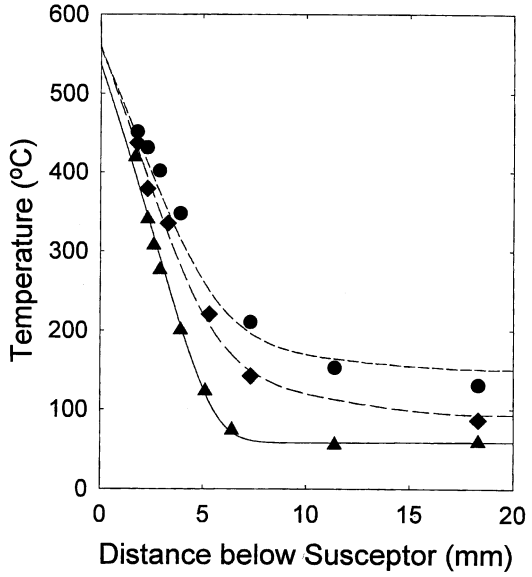


Fig. 4. The axial centerline temperature profiles in the reactor with varying gas inlet velocities for $N_2$ carrier gas: ● $v_0=0.09$ cm $s^{-1}$; ◆, $v_0=1.5$ cm $s^{-1}$; and ▲ $v_0=3.0$ cm $s^{-1}$. Calculated results (solid and dashed lines) are shown with the experimental data: AR=1, $T_{set}=650$ °C.

[32,33] reactor geometries. The result is easily understood by considering the nearly eight times higher thermal conductivity of $H_2$, compared with that of $N_2$.

It is interesting that the extrapolated susceptor surface temperature (537 °C for $N_2$ and 440 °C for $H_2$) is considerably lower than the set point temperature (650 °C). This result suggests that a significant thermal contact resistance exists between the heating block and the inside wall of the quartz furnace housing. The temperature difference observed in the $H_2$ carrier case (210 °C) is close to the one observed by Koppitz et al. [27] using a heater design similar to the one in this study. Their data indicate that the temperature difference between the susceptor surface and the susceptor control temperature is approximately 200 °C at a set point temperature of 727 °C with flowing $H_2$ as the carrier gas. Using a RF-heated graphite susceptor with embedded thermocouples, however, Monteil et al. [32] observed smaller temperature differences (<30 °C). The temperature difference in the $N_2$ case of this study was reduced to a lower value (113 °C) after the furnace was disassembled and reassembled to accommodate the stainless steel spring to provide better physical contact between the heating block and the inside wall of the quartz furnace housing. To better define the surface temperature, the susceptor surface temperature was measured in another experiment using $N_2$ as the carrier gas by bonding a thermocouple directly to the outer surface using a ceramic epoxy. The thermocouple measured a surface temperature of 370 °C, a value lower than the extrapolated surface temperature (537 °C), and considerably lower than the set point temperature. This result is consistent with a significant internal heater/quartz contact resistance and the additional thermocouple contact resistance, along with conductive and convective heat losses along the thermocouple wire. These results emphasize the importance of calibrating the surface temperature, since a large deviation between the measured surface temperature and the control temperature can make the interpretation of growth data and process repeatability difficult.

The measured temperature profile when using $N_2$ as the carrier gas showed that the gas temperature approaches a constant value that is approximately 25 °C higher than room temperature at distances greater than approximately 10 mm from the susceptor. Presumably this was caused by radiation heating of the stainless steel center inlet tube and its packing material which pre-heated the inlet gas. Although it was not possible to measure the inlet temperature in the more conductive $H_2$ carrier gas because the system did not allow probing at distances greater than 18 mm below the susceptor at AR=1, a similar gas pre-heating effect is expected.

The effect of changing the inlet gas velocity on the axial temperature profile in the reactor was investigated for both the $N_2$ (Fig. 4) and $H_2$ carrier gases (Fig. 5). As expected, the decreased residence time in the reactor with increased velocity resulted in a steeper temperature gradient. Cooling of the center tube was also enhanced with higher gas velocity. In the case of the $N_2$ carrier gas, the high temperature zone (>200 °C) was restricted to a distance less than 4.0 mm from the susceptor

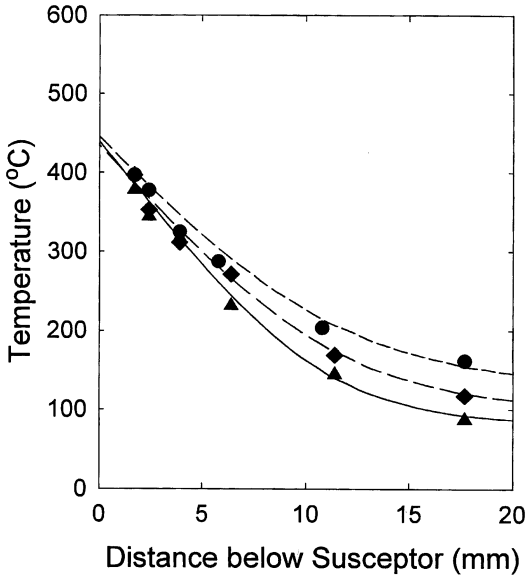


Fig. 5. The axial centerline temperature profiles in the reactor with varying gas inlet velocities for $H_2$ carrier gas: ●, $v_0=0.09$ cm $s^{-1}$; ◆ $v_0=1.5$ cm $s^{-1}$; and ▲ $v_0=3.0$ cm $s^{-1}$. Calculated results (solid and dashed lines) are shown with the experimental data: AR=1, $T_{set}=650$ °C.

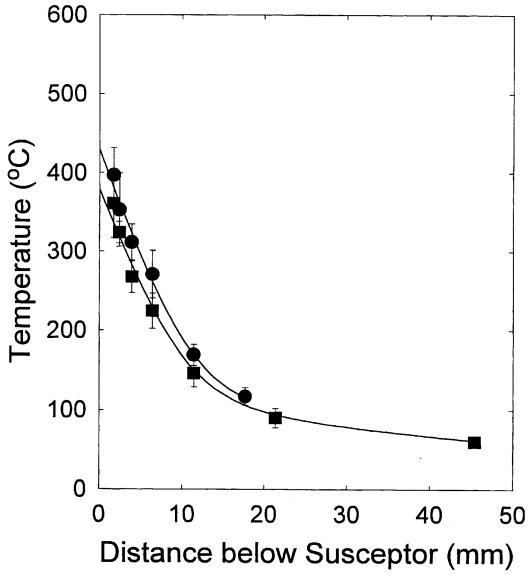


Fig. 6. The effect of varying the aspect ratio (●, AR=1; ■ AR=2) on the axial centerline temperature profile in the reactor for $H_2$ carrier gas. Calculated results (solid lines) are shown with the experimental data: $v_0$=1.5 cm $s^{-1}$ (center and sweeping), $T_{set}$=650 °C.

surface at an inlet velocity of 3.0 cm $s^{-1}$. This narrow high temperature zone near the susceptor was visually observed as a thin cloud of indium droplets when a high concentration of trimethyl indium was introduced into the center flow. In the case of the $H_2$ carrier gas, however, the high temperature zone (>200 °C) thickness was increased to approximately 8.1 mm at the same inlet flow velocity of 3.0 cm $s^{-1}$.

The effect of changing the aspect ratio on the centerline temperature profile was investigated and the results are shown in Fig. 6 when $H_2$ was used as the carrier gas. Increasing the aspect ratio (AR=2) produced a slightly greater temperature gradient, which is attributed to a decrease in radiation heating of the center tube from the hot susceptor. A decrease in the temperature near the center inlet tube was observed with increasing aspect ratio. The shift in the temperature profile produced by increasing the aspect ratio, however, was not large at the operating conditions examined in this study.

## 5. Numerical results and discussion

The results of the numerical calculations are shown in Figs. 3–6 as solid and dashed lines and are compared to the measured temperature values. The calculated results are in good agreement with the experimental results. In these calculations, the heating block (2.74 cm diameter), which was in contact with the inside bottom wall of the furnace, was assumed to be composed of two layers. The top layer was assumed to be at a constant temperature equal to the set point value, and the thermal conductivity of the bottom layer with a fixed thickness of 4.57 mm was adjusted to account for the thermal contact resistance between the heating block and the inside wall of the furnace. The thermal conductivity was varied between 0.8 and 2.1 W $m^{-1}$ $°C^{-1}$, which is within the range of values reported for the thermal conductivity of glass. As stated previously, a large temperature difference (>100 °C) between the control thermocouple at the heating block and the extrapolated surface temperature of susceptor was recorded. This temperature decrease was much larger than that predicted by numerical calculations assuming no contact resistance (36 °C with the $N_2$ carrier gas and 41 °C with the $H_2$ carrier gas at 3.0 cm $s^{-1}$ inlet velocities). Good agreement between the calculated and the experimental temperature profiles was obtained when a thermal contact resistance was included in the simulation.

Including radiation heat transfer in the calculation was found to be necessary to match experimental gas temperatures. The importance of including radiation in the calculation is supported by recent numerical studies [34,35] of a horizontal VPE reactor that indicated the temperature of the upper wall facing the heated susceptor varied by 40–70 K depending on the wall material and the value of the susceptor emissivity. A numerical study of a vertical upflow reactor with a design similar to this study [8] further supports the importance of radiation heat transfer.

Several factors can cause the actual gas dynamics in the reactor to deviate from the calculated results. For example, in real reactors, purely axisymmetric boundary conditions cannot be achieved (e.g. alignment of the center inlet tube, temperature variations across the susceptor surface). Sharp corners and sudden expansions (or contractions) in the flow cross-sectional area can also produce laminar vortices. The two-dimensional analysis performed in this study, however, provides insight into the gas dynamics in the reactor, and it successfully represents the experimentally measured axial temperature profile when using reasonable boundary conditions.

Figs. 7 and 8 show the calculated streamlines and isotherms in the reactor as a function of the inlet flow velocity using $N_2$ and $H_2$ carrier gases, respectively. At the very low inlet flow velocity (0.09 cm $s^{-1}$), the isotherms spread toward the gas inlet for both $N_2$ (Fig. 7b) and H (Fig. 8b), indicating a relatively small temperature gradient normal to the susceptor surface. Recirculation flow patterns are produced at this velocity by the transverse thermal gradient. A more complex recirculation structure was observed in the $N_2$ carrier gas (Fig. 7a), as compared to that in the $H_2$ carrier gas (Fig. 8a), because the side wall heating is greater when using $N_2$. As the inlet flow velocity increases to 3.0 cm $s^{-1}$, the isotherms contract toward the susceptor (Fig. 7d and Fig. 8d), and the fluid flow becomes simpler as

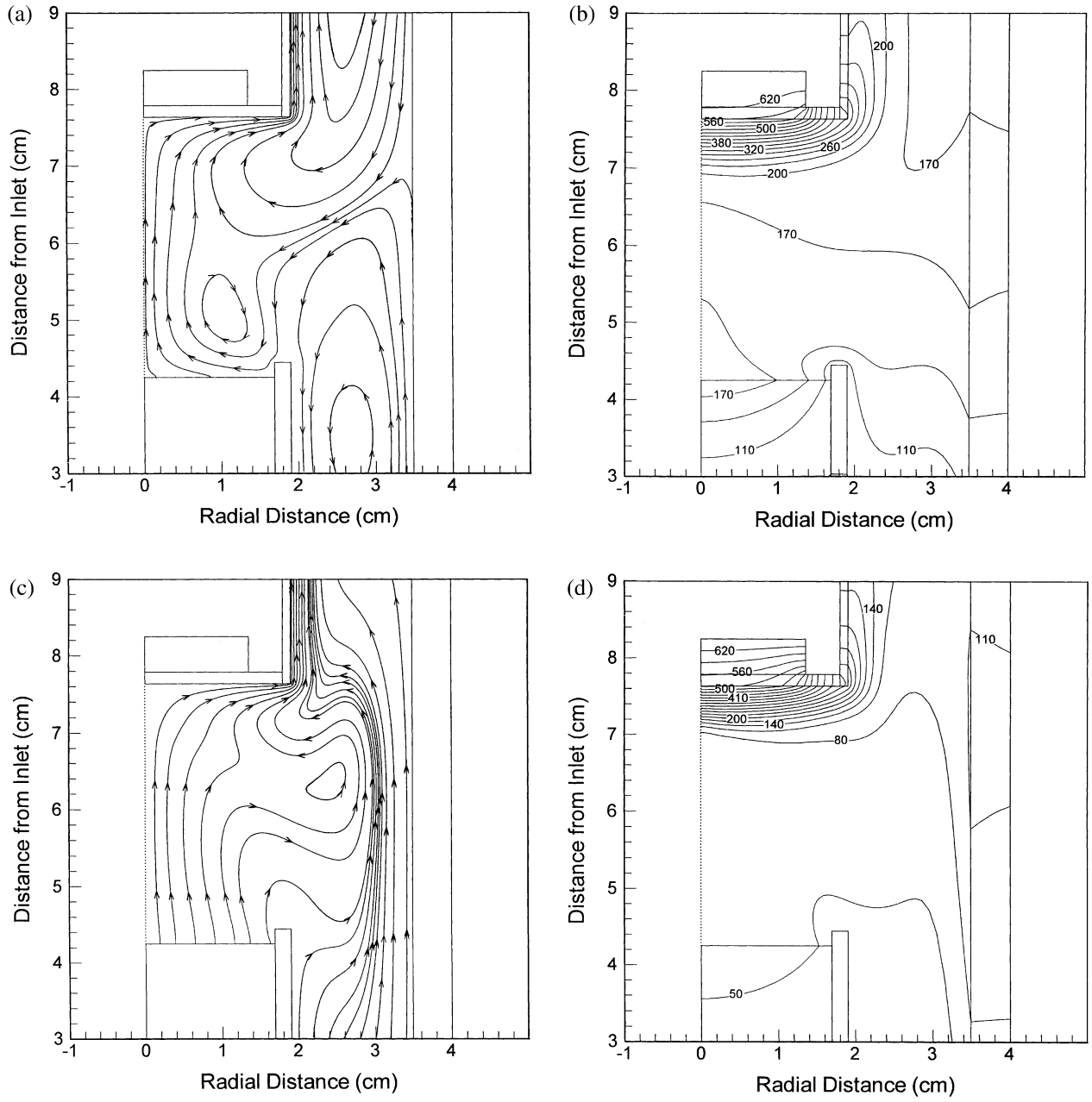


Fig. 7. Calculated streamlines and isotherms in the reactor for $N_2$ carrier gas as a function of the gas inlet velocity: (a) streamlines and (b) isotherms for $v_0 = 0.09$ cm s$^{-1}$ (center and sweeping); (c) streamlines; and (d) isotherms for $v_0 = 3.0$ cm s$^{-1}$ (center and sweeping). $T_{set} = 650$ °C. The temperature spacing between adjacent isotherms is 30 °C.

forced convection dominates (Fig. 7c and Fig. 8c). The isotherms are more confined to the vicinity of the susceptor and are parallel to the susceptor at the highest velocity studied with the use of an $N_2$ carrier gas (Fig. 7d). The isotherms developed in the reactor with the use of the more conductive $H_2$ carrier gas, however, were not confined to the vicinity of the susceptor even at the highest velocity studied (3.0 cm s$^{-1}$). The recirculation flow patterns were not as strong in the entire operating range used in this study, except for the case with very small gas velocity (0.09 cm s$^{-1}$), for both $N_2$ and $H_2$ carrier gases. The numerical results indicate that the $H_2$ carrier gas provides more stable flow profiles than the $N_2$ carrier gas at the same matched inlet velocities. The higher thermal conductivity of $H_2$ reduces the transverse thermal gradients, and therefore, natural convection is weaker. The upflow reactor geometry used in this study and the relatively low susceptor temperature appear to be responsible for the prediction of only weak recirculation flow patterns. To support this conclusion, simulations were performed with the same reactor geometry, but oriented in the direction of the

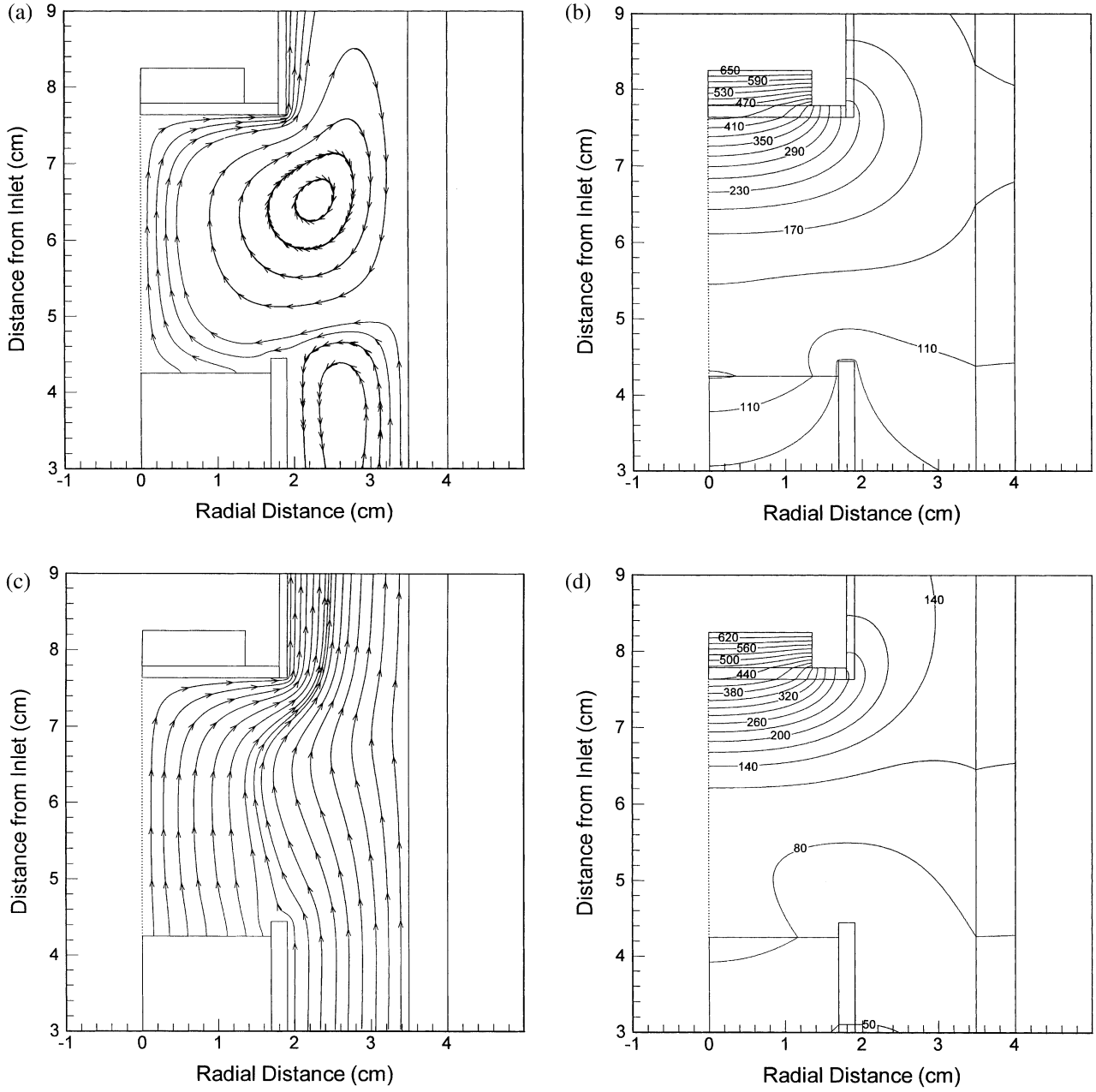


Fig. 8. Calculated streamlines and isotherms in the reactor for $H_2$ carrier gas as a function of the gas inlet velocity: (a) streamlines and (b) isotherms for $v_0 = 0.09$ cm $s^{-1}$ (center and sweeping); (c) streamlines; and (d) isotherms for $v_0 = 3.0$ cm $s^{-1}$ (center and sweeping). $T_{set} = 650$ °C. The temperature spacing between adjacent isotherms is 30 °C.

gravity vector. The results for $H_2$ are shown in Fig. 9. At an inlet velocity of 3.0 cm $s^{-1}$, a strong flow recirculation pattern exists (Fig. 9a) and the isotherms spread out towards the gas inlet (Fig. 9b). The flow recirculation patterns became more complex and stronger for the $N_2$ carrier gas. These results clearly indicate the effect of the inverted design on suppressing flow recirculation.

From the viewpoint of the gas dynamics, the use of an $N_2$ carrier gas at high velocity seems to be preferred for the growth of epitaxial layers. Isotherms confined and parallel to the substrate surface help prevent parasitic phase reactions, and uniform flow fields allow more uniform mass transfer. The work of Sacilotti et al. [36] showed that more uniform epitaxial layers were deposited in the deposition of InP from $In(CH_3)$ and $PH_3$, in a horizontal reactor when $N_2$ was used as the carrier gas as compared to $H_2$. Other problems such as the purity of the $N_2$ carrier gas and the positive role of $H_2$ in the deposition chemistry (e.g. reducing carbon incorporation by reaction with methyl radicals), however, must be considered when selecting the carrier gas. From

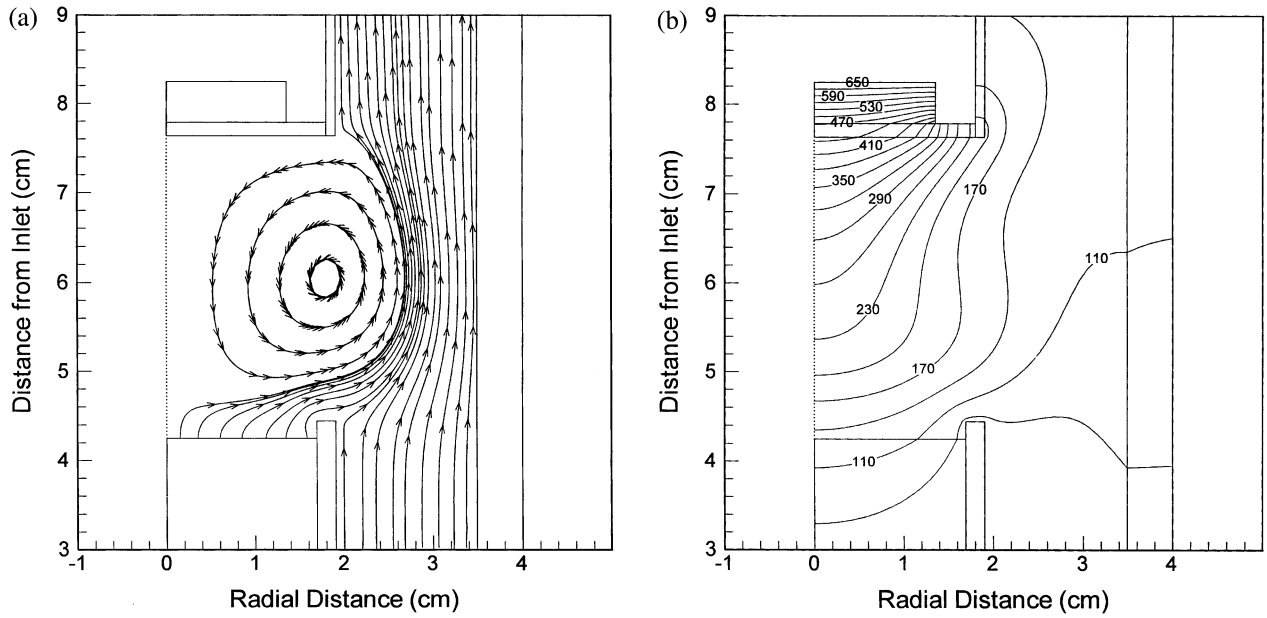


Fig. 9. Calculated streamlines and isotherms in the reactor for $H_2$ carrier gas when the gravity is inverted: (a) streamlines and (b) isotherms for $v_0 = 3.0$ cm s$^{-1}$ (center and sweeping). $T_{set} = 650$ °C. The temperature spacing between adjacent isotherms is 30 °C.

the perspective of gas dynamics in a vertical reactor, the upflow reactor configuration is preferred, since it can more easily provide forced convection dominated flow fields due to the stabilizing density gradient developed in the reactor. It also provides a more favorable arrangement for particle rejection. Substrate handling issues related to automation, however, need to be carefully addressed for successful operation.

## 6. Summary

Temperature profiles in a vertical upflow, cold-wall CVD reactor were measured by analysis of the pure rotational Raman scattering from diatomic carrier gas molecules. It was found that a larger temperature gradient normal to the susceptor surface is obtained with a higher gas flow velocity, larger aspect ratio and the use of $N_2$ carrier gas. A two-dimensional axisymmetric model was developed, and the calculated results were compared with experimental data. Good agreement between the measured and calculated temperature profiles was obtained when corrections were made to the thermal boundary conditions. Careful treatment of heat transfer was found to be critical in obtaining realistic predictions. Calculations suggested that buoyancy-driven recirculation flows were non-existent or weak in the studied velocity and temperature ranges. The stabilizing density gradient provided by the upflow geometry is a positive characteristic of this reactor geometry.

## Acknowledgments

The authors would like to thank Dr Z.S. Huang, Dr Alex Zhao, Dr W.S. Jung and Mr P. Axson for their helpful discussions. This work is supported in part by KOSEF Grant #96-0300-14-01-3.

## References

[1] J.P. Hirtz, M. Razeghi, M. Bonnet, J.P. Duchemin, in: T.P. Pearsall (Ed.), GaInAsP Alloy Semiconductors, Ch. 3, John Wiley and Sons, New York, NY, 1982.
[2] G.B. Stringfellow, Organometallic Vapor Phase Epitaxy: Theory and Practice, Academic Press, San Diego, CA, 1989.
[3] K.F. Jensen, J. Cryst. Growth 98 (1989) 148.
[4] L.J. Giling, J. Electrochem. Soc. 129 (1982) 634.
[5] D.J. Fotiadis, S. Kieda, K.F. Jensen, J. Cryst. Growth 102 (1990) 441.
[6] K.F. Jensen, D.I. Fotiadis, T.J. Mountziaris, J. Cryst. Growth 107 (1991) 1.
[7] S. Patniak, R.A. Brown, C.A. Wang, J. Cryst. Growth 96 (1989) 153.
[8] P.B. Chinoy, D.A. Kaminski, S.K. Ghandhi, Solar Cells 30 (1991) 323.
[9] G. Wahl, Thin Solid Films 40 (1977) 13.
[10] P. Lee, D. McKenna, D. Kapur, K.F. Jensen, J. Cryst. Growth 77 (1986) 120.
[11] C.A. Wang, S.H. Groves, S.C. Palmateer, D.W. Weyburne, R.A. Brown, J. Cryst. Growth 77 (1986) 136.
[12] Yu.N. Makarov, A.I. Zhmakin, J. Cryst. Growth 94 (1989) 537.
[13] A.I. Gurary, G.S. Tompa, A.G. Thompson, R.A. Stall, P.A. Zawadzki, N.E. Schumaker, J. Cryst. Growth 145 (1994) 642.
[14] G.S. Tompa, P.A. Zawadzki, K. Moy, M. Mckee, A.G. Thompson, A.I. Gurary, E. Wolak, P. Esherk, W.G. Breiland, G.H. Evans, N. Bulitka, J. Hennessy, C.J.L. Moore, J. Cryst. Growth 145 (1994) 655.
[15] C. Houtman, D.B. Graves, K.F. Jensen, J. Electrochem. Soc. 133 (1986) 961.
[16] D.I. Fotiadis, A.M. Kremer, D.R. McKenna, K.F. Jensen, J. Cryst. Growth 85 (1987) 154.

[17] S.I. Boldish, J.S. Ciofalo, J.P. Wendt, J. Electron. Mater. 14 (1985) 587.
[18] V.S. ban, J Electrochem. Soc. 125 (1978) 317.
[19] L.J. Giling, J. Physique 43 (1982) C5–235.
[20] D.A. Long, Raman Spectroscopy, McGraw-Hill, New York, NY, 1986.
[21] H.W. Schrötter, H.W. Klöckner, in: A. Weber (Ed.), Raman Spectroscopy of Gases and Liquids, Ch. 4, Berlin, 1979.
[22] R.C. Weast (Ed.), Handbook of Chemistry and Physics, 67th ed, CRC Press, Boca Raton, FL, 1987.
[23] J.H. Keenan, J. Chao, J. Kaye, Gas Tables, 2nd ed, John Wiley and Sons, New York, NY, 1980.
[24] J.D. Ingle, S.R. Crouch, Spectrochemical Analysis, Prentice Hall, Upper Saddle River, NJ, 1988, p. 522.
[25] R. Siegel, J.R. Howell, Thermal Radiation Heat Transfer, McGraw-Hill, New York, NY, 1972, p. 190.
[26] J.C. Heinrich, S. Marshall, Computers Fluids 9 (1981) 73.
[27] M. Koppitz, O. Vestavik, W. Pletschen, A. Mircea, M. Heyen, W. Richter, J. Cryst. Growth 68 (1984) 136.
[28] H. Moffat, K.F. Jensen, J. Cryst. Growth 77 (1986) 108.
[29] L. Stock, W. Richter, J. Cryst. Growth 77 (1986) 144.
[30] J. Van de Ven, G.M.J. Rutten, M.J. Raaijmakers, L.J. Giling, J. Cryst. Growth 76 (1986) 352.
[31] D.I. Fotiadis, M. Boekholt, K.F. Jensen, W. Richter, J. Cryst. Growth 100 (1990) 577.
[32] Y. Monteil, M.P. Berthet, R. Favre, A. Hariss, J. Bouix, M. Vaille, P. Gibart, J. Cryst. Growth 77 (1986) 172.
[33] Y. Monteil, R. Favre, A. Bekkaoui, P. Raffin, J. Bouix, J. Marcillat, P. Dutto, J. Cryst. Growth 93 (1988) 270.
[34] L. Kadinski, Yu.N. Makarov, M. Schäfer, M.G. Vasil'ev, V.S. Yuferev, J. Cryst. Growth 146 (1995) 209.
[35] F. Durst, L. Kadinski, M. Schäfer, J. Cryst. Growth 146 (1995) 202.
[36] M. Sacilotti, A. Mircea, R. Azoulay, J. Cryst. Growth 63 (1983) 111.